DETECTING SPACE OBJECTS WITH BINARY WIDE FIELD OF VIEW X-RAY SENSING

Andrea Lopez[*], Julian Hammerl[†], and Hanspeter Schaub[‡]

Passive detection of objects in the vicinity of a spacecraft is beneficial for a variety of applications, including collision avoidance, proximity operations, and relative navigation. The x-rays generated from ambient space environment electrons impacting an object provide the means for detecting the object over a range of distances depending on local plasma properties. This work investigates the use of a wide field of view x-ray detector solution composed of a cluster of commercial narrow field of view sensors. In this study, the target is assumed to be far enough away such that only a binary on-off signal is detected if the object is within the field of view of a sensor. The cluster is mounted on a rotating platform to detect and track objects in the vicinity of a spacecraft. Acquisition and loss of signal events are used to provide a least-squares solution for the heading of the incoming signal. The results show that there is a trade-off between amount of coverage and average error in the covered area, so the ideal configuration geometry depends on the specific application. Due to the rotation of the sensors, the direction normal to the cluster platform is always unobservable, leading to blind spots. Using multiple clusters of sensors eliminates such blind spots, and increases coverage while improving the average error.

INTRODUCTION

Spacecraft in geostationary orbits (GEO) provide a vital communications and surveillance role, but they operate in a domain where defunct spacecraft and debris accumulation are a risk factor. Furthermore, this region can be difficult to monitor with ground-based systems.[1] Future trends for a sustainable exploitation of this region include on-orbit servicing procedures.[2] Strategic interest in the Moon and cislunar space is growing for private companies and government agencies, with on-orbit assembly and proximity operations being a crucial step in prospective missions.[2,3] Passive object detection and tracking in the proximity of a spacecraft is an asset for a wide range of applications, including On Orbit Servicing, Assembly and Manufacturing (OSAM), Space Situational Awareness (SSA), and Space Traffic Management (STM).

Energetic electrons in the ambient plasma interact with any object in space, inducing the emission of x-rays. These plasma environments are present in regions such as GEO and cislunar space. The x-ray spectrum generated consists of bremsstrahlung radiation and characteristic x-rays. The

---

[*]PhD Student, Ann and H.J. Smead Department of Aerospace Engineering Sciences, University of Colorado, Boulder, Boulder, CO, 80309. AIAA Student Member.

[†]PhD Student, Ann and H.J. Smead Department of Aerospace Engineering Sciences, University of Colorado, Boulder, Boulder, CO, 80309. AAS Student Member, AIAA Student Member.

[‡]Professor and Department Chair, Schaden Leadership Chair, Ann and H.J. Smead Department of Aerospace Engineering Sciences, University of Colorado, Boulder, 431 UCB, Colorado Center for Astrodynamics Research, Boulder, CO, 80309. AAS Fellow, AIAA Fellow.
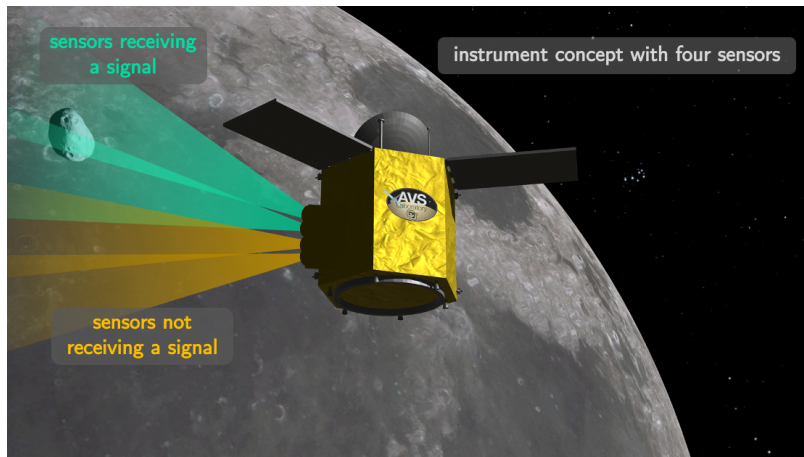
Figure 1: Four-sensor instrument concept, with two sensors detecting a nearby object

wavelength of the latter is specific to the element of origin, which allows rapid assessment of the material composition of an object by spectral signature.[4] Bremsstrahlung radiation has been previously used to remotely estimate the electrical potential of an object, utilizing x-ray detectors in combination with an electron gun to excite x-ray emissions of a known target.[5,6] This work investigates the use of a wide field of view (FOV) x-ray detection solution that exploits the natural space environment interactions to detect and track objects neighboring a spacecraft. The x-ray detection capabilities depend on local plasma properties but are not contingent on illumination conditions. This potentially presents an advantage over visible light detection methods as it functions in the Moon's shadow and eclipse regions. The proposed sensor consists of a cluster of off-the-shelf x-ray detectors with partially overlapping FOVs, motivated by a coarse sun sensor assembly concept (see Figure 1). This cluster is then mounted on a platform that is rotating at a constant speed. The events of *signal acquisition* and *loss of signal* are used to estimate the heading of the incoming x-ray signal, providing the means to locate the target object passively.

This work investigates the case of a stationary target with respect to the spacecraft. The signal at each detector is modeled as an on/off step signal, with a value of 1 if the target is visible by the sensor, and 0 otherwise (see Figure 2). The acquisition/loss of signal events are generated by the motion of the rotating platform with respect to the spacecraft. The baseline algorithm for the estimation of the heading uses these triggers to locate the target object, employing a least squares method.

A number of detector configurations for a cluster of x-ray sensors are discussed. The efficiency of each configuration is analyzed by comparing two performance metrics, *coverage* and *average error* in the area covered. The design space for a cluster of two, three, four or six sensors is then examined, for changing values of FOV of the individual sensors, and angular separation of the sensors.

Next, an instrument concept consisting of multiple x-ray clusters is considered. Given a fixed number of 12 x-ray sensors, four study cases are investigated: two clusters of six sensors, three clusters of four sensors, four clusters of three sensors, and six clusters of two sensors. These clusters are positioned such that the 2π steradians around the instruments preferred direction are fully covered. Coverage and average error are again calculated and the four cases are compared.
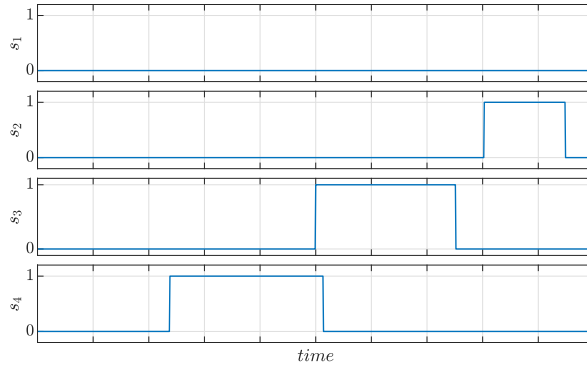
Figure 2: Example of signals detected by fours sensors after a full rotation for an arbitraty target

PROBLEM STATEMENT

Methodology

In this work, the target is modeled as a point source which remains stationary with respect to the observer spacecraft. For each of the sensors, the signals are modeled as step functions, with a value of 0 when no signal is being observed (target outside of the field of view of the sensor), and 1 when an object is within sight of the sensor (see Figure 2). Although this is a very simplistic model of the signal behavior, when combining the observations of multiple sensors it is possible to obtain an accurate heading for the target object.

The acquisition or loss of signal triggers are then used to solve for the heading of the target with respect to the spacecraft. Therefore, at the time of a trigger event,

$$\boldsymbol{s}_i^{*T} \cdot \boldsymbol{h} = \cos f \tag{1}$$

where $\boldsymbol{s}_i^*$ is the unit normal of sensor i at the time of the trigger, f is the half angle of the field of view cone and $\boldsymbol{h}$ is the unit heading of the target.

Combining multiple trigger events into matrix form

$$\begin{bmatrix} \boldsymbol{m}_1^T \\ \boldsymbol{m}_2^T \\ \vdots \\ \boldsymbol{m}_p^T \end{bmatrix} \cdot \boldsymbol{h} = \begin{bmatrix} \cos f \\ \cos f \\ \vdots \\ \cos f \end{bmatrix} \tag{2}$$

with $\boldsymbol{m}_j$ the jth measurement obtained from any of the sensors $\boldsymbol{s}_i^*$, and p the total number of measurements. In general, the measurements obtained are not perfect and may have errors with respect to the *true measurements* (*e.g.,* pointing errors/biases in the sensors).

The measurement equation is now in the classic matrix-vector form

$$A\boldsymbol{x} + \boldsymbol{\epsilon} = \tilde{\boldsymbol{y}} \tag{3}$$

with A the matrix of $\boldsymbol{m}_j$, $\boldsymbol{x} = \boldsymbol{h}$ the state to be estimated, $\boldsymbol{\epsilon}$ a vector of measurement errors, and $\tilde{\boldsymbol{y}}$ the vector of $\cos \tilde{f}$.

The solution to this equation is

$$\hat{\boldsymbol{x}} = A^{+}\tilde{\boldsymbol{y}} \tag{4}$$

where A^{+} is the Moore-Penrose inverse of matrix A. In scenarios where $rank(A) \geq 3$, Equation (4) provides the least squares solution to the problem. If $rank(A) < 3$, meaning there are two or fewer unique measurements, the problem is under-determined and Equation (4) provides the minimum norm solution. In both cases the resulting $\hat{\boldsymbol{x}}$ constitutes the best estimate of the state.

Target signal intensity

In order to detect when the target enters and exits the field of view of an x-ray sensor (acquisition/loss of signal), the x-rays received from the target object must be higher in intensity than the x-ray background noise. The total number of photons per second received from an aluminum target with area A_{SC} at a distance d is approximated using theoretical x-ray models, and compared to the count rates of solar x-rays scattered from the lunar surface and the count rate of the cosmic diffuse x-ray background (DXRB).

References 7 and 8 are used to approximate the characteristic x-ray and bremsstrahlung radiation, respectively, generated at the target per incident electron with energy E_e. These empirical x-ray models assume thick targets, *i.e.,* it is assumed that the incident electron is fully stopped within the material. Reference 9 provides the IGE-2006 electron flux model at geostationary orbit for electron energies between 1 keV and 5.2 MeV. Using the electron flux from the IGE-2006 model for mean solar activity, the theoretical x-ray spectrum emitted from the target due to the impacting ambient plasma electrons is generated, and the total number of photons per second computed by integrating over all photon energies E_p. However, these x-rays are emitted in all directions, and only a fraction $\Omega = A_{\text{det}}/d^2$ is received by the sensor, where A_{det} is the area of the x-ray sensor. The energy dependent efficiency of the sensor* is also considered, as low energy photons are attenuated by the frontal window of an x-ray detector. While the electron flux model is for geostationary orbit, to compare the signal with the background noise the spacecraft is assumed to be in a lunar orbit with an altitude of 1000 km, assuming that the x-rays emitted due to the ambient plasma are similar in intensity in both regions. For a target with area $A_{SC} = 10$ m^2 at a distance $d = 500$ m away from the spacecraft, the obtained count rate is $I_t = 1.69$ photons/s with an x-ray sensor area of $A_{\text{det}} = 75$ mm^2.

The count rates of the background noise obtained by the ROSAT spacecraft are 15 photons/s for the bright side of the Moon, 0.2 photons/s for the dark side of the Moon, and 6 photons/s for DXRB.[10] The ROSAT x-ray telescope was situated in low earth orbit, with a telescope diameter of 84 cm (area of the telescope $A_{\text{tel}} = 2.22$ m^2). Thus, for an approximation, the lunar surface count rates are multiplied by $F_1 = A_{\text{det}}/A_{\text{tel}} \cdot (r_{ME}/r_{MS})^2$ and the DXRB count rate is multiplied by $F_2 = A_{\text{det}}/A_{\text{tel}}$ to account for the different sensor areas and distances from the Moon. The distance r_{ME} between the Moon and Earth is assumed to be $384,000$ km and the distance between the lunar surface and the spacecraft is 1000 km. With these adjustments, the approximate background noise count rates sensed by the x-ray detector are $I_{M,b} = 74.84$ photons/s for the bright side of the Moon, $I_{M,d} = 0.99$ photons/s for the dark side of the Moon, and $I_{DXRB} = 2.03 \times 10^{-4}$ photons/s for DXRB.

---

*https://www.amptek.com/products/x-ray-detectors/sipin-x-ray-detectors/sipin-x-ray-detectors (Consulted on: 07/22/2022)

According to this approximation, the signal $I_t = 1.69$ photons/s received from the target object is orders of magnitudes stronger than the cosmic diffuse x-ray background, while it is similar in intensity as the x-rays coming from the lunar dark side and lower in intensity than the x-rays scattered from the lunar bright side. This suggests that the proposed x-ray wide FOV detector solution could be impaired if the Moon is in the field of view of the sensors. However, if the spacecraft is farther away from the Moon or if the Moon is not in the field of view, the signal from the target is strong enough compared to the background noise to trigger acquisition/loss of signal events.

SINGLE CLUSTER

This section explores different possible configurations for an x-ray sensor cluster. Because the scenario described here consists of a target that is static as viewed from the spacecraft, a sensor cluster with a fixed orientation would result in no acquisition or loss of signal events or, in other words, zero measurements of the target. In dynamic scenarios with the target following an arc as seen by the spacecraft, this would result in a handful of triggers at most. Aiming to increase the number of observations, and therefore improve the heading estimation capabilities, the sensors are mounted on a rotating platform. The platform coordinate frame is defined as $\mathcal{P} : \{\boldsymbol{p}_1, \boldsymbol{p}_2, \boldsymbol{p}_3\}$, with $\boldsymbol{p}_3 = \boldsymbol{n}_P$ the unit vector normal to the platform. Here, this platform is assumed to be rotating with angular velocity $\boldsymbol{\omega} = \omega \boldsymbol{n}_P$, where $\omega = const.$ is the rotational speed. The position of the sensors $\boldsymbol{s}_i$ is fixed in the platform frame $\mathcal{P}$. Therefore, to obtain the sensor pointing with respect to the spacecraft body frame $\mathcal{B}$ at time t

$$
{}^{\mathcal{B}}\boldsymbol{s}_i(t) = \begin{bmatrix} \cos \omega t & -\sin \omega t & 0 \\ \sin \omega t & \cos \omega t & 0 \\ 0 & 0 & 1 \end{bmatrix} {}^{\mathcal{P}}\boldsymbol{s}_i = [BP]\,{}^{\mathcal{P}}\boldsymbol{s}_i \tag{5}
$$

with ${}^{\mathcal{P}}\boldsymbol{s}_i$ the sensor pointing vector in the $\mathcal{P}$ frame, ${}^{\mathcal{B}}\boldsymbol{s}_i(t)$ the sensor pointing vector in the $\mathcal{B}$ frame, and $[BP]$ the time varying direction cosine matrix (DCM) of the rotation.

The pointing of each sensor with respect to the cluster platform is defined with azimuth and elevation angles. Azimuth is measured positive from the platform positive $\boldsymbol{p}_1$ axis around the $+\boldsymbol{n}_P$ axis, and elevation is measured positive toward the platform $\boldsymbol{n}_P$ axis from the $p_1 p_2$ plane, as shown in Figure 3. The *preferred direction* for the instrument to have coverage is defined here as the positive $\boldsymbol{z}$ spacecraft axis. For this section, the cluster platform is assumed to be mounted on the $+z$ side of a spacecraft, and therefore $\boldsymbol{n}_P$ is aligned with the spacecraft $\boldsymbol{z}$ axis.

$$
{}^{\mathcal{P}}\boldsymbol{s}_i = \begin{bmatrix} \cos \theta_i \cos \phi_i \\ \sin \theta_i \cos \phi_i \\ \sin \phi_i \end{bmatrix} \tag{6}
$$

Note that, unlike for cosine-type coarse sun sensors (CSS),[11, 12] the signal here is not modeled with a cosine law but as a step function. Large edge-to-edge fields of view ($\sim 120°$) are not as advantageous here and, in order to limit stray light and scattering generating spurious signals, sensors are assumed to incorporate baffles that limit the field of view from $f = 4°$ to $40°$ half angle depending on the case.

Pyramid configuration

The cluster of x-ray sensors instrument concept is inspired by CSS assemblies,[13] so the initial configuration analyzed for this concept is a classic four-sensor pyramid configuration, named here
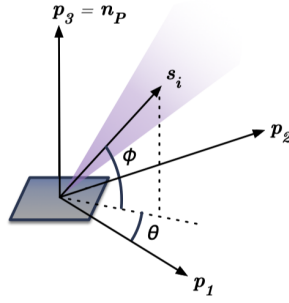
Figure 3: Azimuth and elevation angles with respect to cluster platform
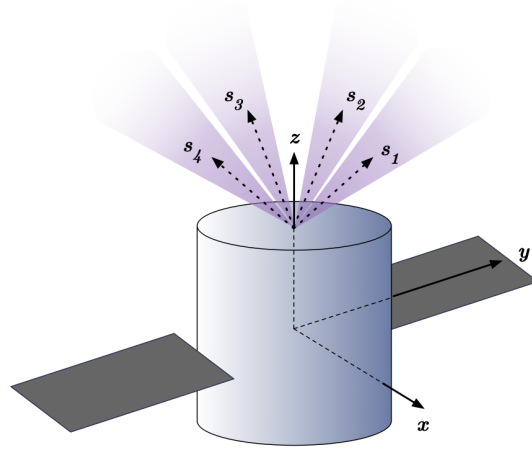

Figure 4: Illustration of a four-sensor instrument concept in pyramid configuration

configuration A. In this configuration, the sensors are oriented $90°$ apart and angled $45°$ from the normal of the spacecraft side. An illustration of this configuration is shown in Figure 4, for an instrument located on the $+z$ face of the spacecraft.

Table 1: Azimuth and elevation angles of x-ray sensors in pyramid configuration

Sensor	θ [deg]	ϕ [deg]
1	0	45
2	90	45
3	180	45
4	270	45

A list of the azimuth and elevation angles used for this configuration is shown in Table 1. Figure 5a shows how many sensors can detect a target in a given point and Figure 5b shows the errors obtained for the heading of a target in Lambert cylindrical projection[14] of the 2π sr in the $+z$ direction. Because the platform is rotating about its normal, the problem is axisymmetric about the rotation axis, meaning that the results are constant for all azimuth angles. Therefore the grid can be reduced to a single arbitrary azimuth value, and Figure 5 can be summarized in a single plot in Fig-
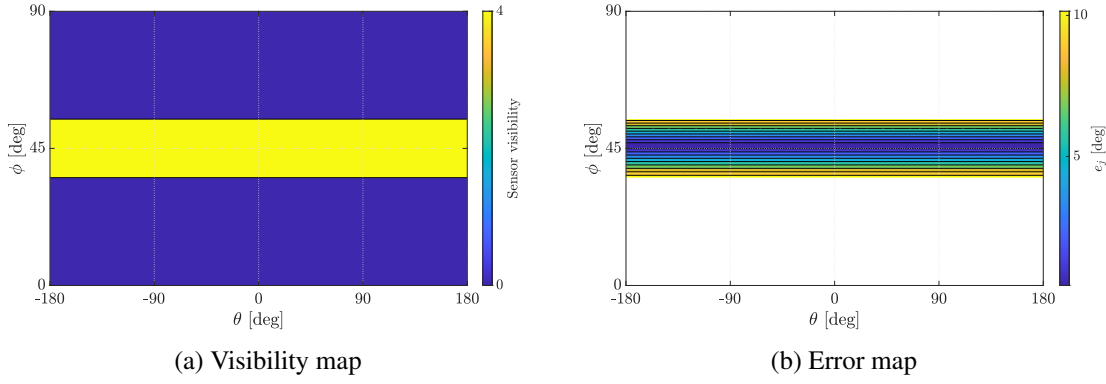
(a) Visibility map   (b) Error map

Figure 5: Visibility of a target and error obtained in the hemisphere of interest
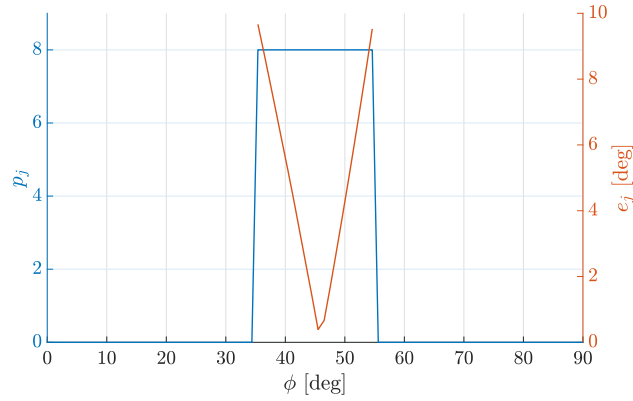

Figure 6: Number of measurements p_j (blue) and error e_j (red) with target elevation for configuration B, arbitrary azimuth angle

ure 6. This also implies that the present configuration in which all sensors have the same elevation angle is not a suitable configuration. The additional sensors do not provide any further information, but only add repeated measurements. Therefore under this configuration the maximum number of unique measurements obtainable is 2: one measurement when the signal is acquired and another measurement when the signal is lost. Thus, the problem is essentially under-determined.

In order to compare the capabilities of the different configurations, two performance metrics are defined: coverage and average error. With this purpose, the observation surface considered (2π sr in the $+z$ direction of the platform) is discretized in azimuth and elevation $[-180°, 180°] \times [0°, 90°]$, with a grid resolution of $0.5° \times 0.5°$.

Coverage is defined as

$$cvg = \frac{n_m}{n_T} \tag{7}$$

with n_m the number of points in the grid where at least one measurement is available, and n_T the total number of grid points (with the given grid definition, $n_T = 720 \cdot 180 = 129600$ points). The coverage obtained for this configuration is $cvg_A = 0.222$.
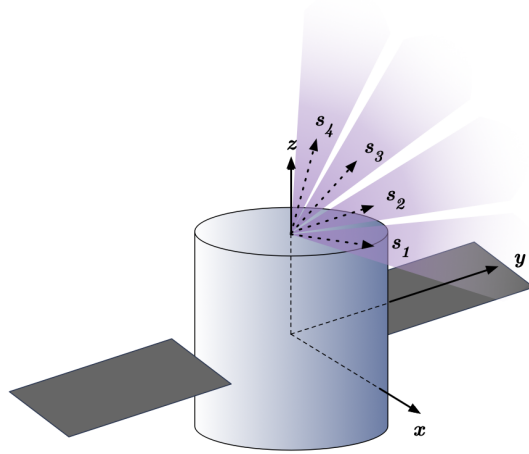
7

Figure 7: Illustration of a four-sensor instrument concept in elevation distributed configuration

Average error is defined as

$$\bar{e} = \frac{\sum\limits_{j=1}^{n_m} e_j}{n_m} \tag{8}$$

where $e_j = \arccos\left(\hat{\boldsymbol{x}}^T \boldsymbol{x}\right)$ is the angle between the estimated and true heading of the target in degrees at grid point j. The average error obtained for this pyramid configuration is $\bar{e} = 5.06°$.

By discretizing in azimuth and elevation, an area with no coverage or larger errors around the zenith has a larger weight in the performance metrics than a same sized area with a lower elevation. This grid definition is therefore consistent with having a preferred direction at $\phi = 90°$, around which having a diminished performance will greatly affect the defined metrics of coverage and average error.

Elevation distributed configurations

The rotation of the platform prescribed to increase the number of trigger events makes the pyramid configuration particularly inadequate for this problem, providing a maximum of two unique measurements in the considered hemisphere. Rather than opting for more complicated platform options that increase the complexity of the system, different sensor configuration are analyzed, in which each of the sensors has a different elevation. An illustration of this concept is shown in Figure 7.

Figure 8 shows the number of measurements p_j and error e_j obtained at each point of the grid for a configuration of sensors with $f = 10°$ distributed in elevation, named configuration B. Table 2 shows the azimuth and elevation of this configuration of sensors. Here, the separation between the sensors is $20°$ and therefore they do not overlap.

With the sensors not overlapping, only one sensor detects a target object with elevation between $10°$ and $90°$, and only two unique measurements are obtained (*i.e.,* signal acquisition and loss of signal). The problem is therefore under-determined, and the solution found for any given point is
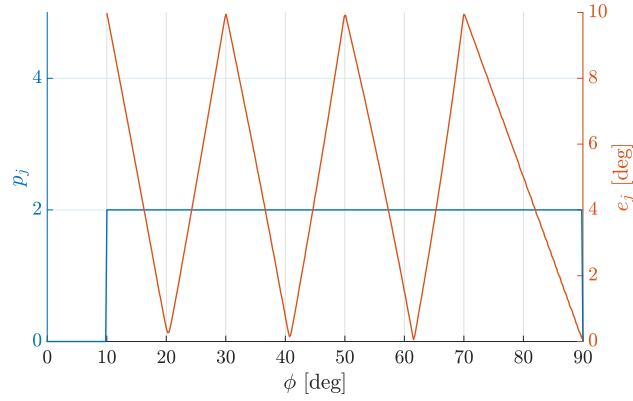
Figure 8: Number of measurements p_j (blue) and error e_j (red) with target elevation for configuration B, arbitrary azimuth angle

Table 2: Azimuth and elevation angles of x-ray sensors for configuration B

Sensor	θ [deg]	ϕ [deg]
1	0	20
2	0	40
3	0	60
4	0	80

the minimum norm solution. The coverage for configuration B is $cvg_B = 0.88$ and the average error is $\bar{e}_B = 5.03°$.

Figure 9 shows the number of measurements p_j and error e_j for a configuration of sensors with $f = 10°$ distributed in elevation, in this case with overlapping fields of view, named configuration C. Table 3 shows the azimuth and elevation angles for the four sensors. Although the area covered is significantly smaller (ϕ from $40°$ to $90°$), this overlaps ensures a two sensor coverage between $\phi = 50°$ and $80°$. Thus, in this region the problem is fully determined. The coverage for configuration C is $cvg_C = 0.55$ and the average error is $\bar{e}_C = 1.67°$.

Table 3: Azimuth and elevation angles of x-ray sensors for configuration C

Sensor	θ [deg]	ϕ [deg]
1	0	50
2	0	60
3	0	70
4	0	80

Depending on the application, coverage may be prioritized over average error or vice versa, requiring the separation between sensors to increase or decrease accordingly. The field of view of the individual sensors also plays a role in coverage and average error results for a given sensor separation. To gain a better understanding of how these parameters affect the performance of the instrument, an analysis of the design space is performed.
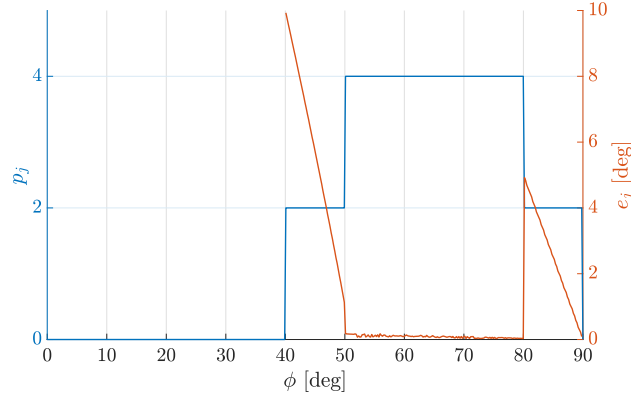
9

Figure 9: Number of measurements p_j (blue) and error e_j (red) with target elevation for configuration C, arbitrary azimuth angle
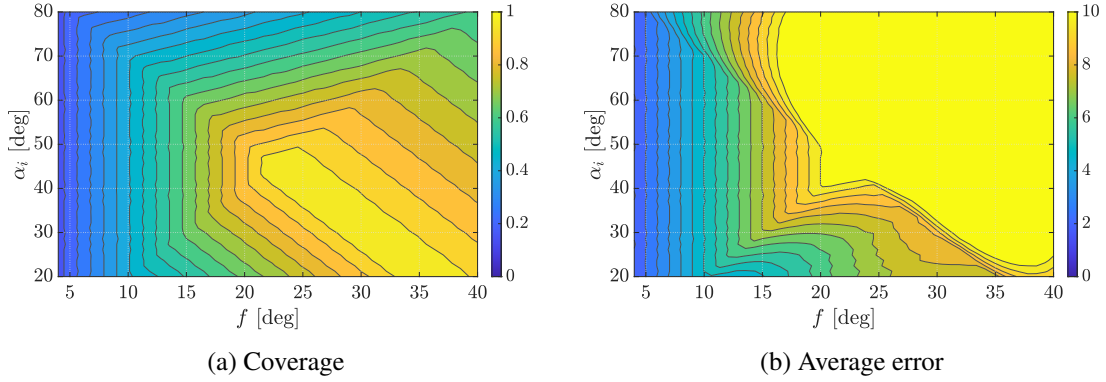

(a) Coverage

(b) Average error

Figure 10: Design space for a cluster concept of two x-ray sensors

Design space study

For a given number of sensors, with the sensors distributed evenly in elevation, there are two main parameters of interest for the design space: field of view of the individual sensors and angular separation in elevation between consecutive sensors. The two metrics considered here to designate a good design point are coverage and mean error in the covered area. In order to obtain a comprehensive understanding of the design space, a grid of points for field of view $f \in [4°, 40°]$ and total angular spread $\alpha_t \in [20°, 80°]$ is defined. This total angular spread α_t is the difference between the first and last sensor elevation $\alpha_t = \phi_N - \phi_1$. The individual angular spread between two consecutive sensors is then $\alpha_i = \frac{\alpha_t}{N-1}$. The design metrics of coverage and average error are then computed for every point of the grid using Equations 7 and 8, respectively. The results of the design space analysis for clusters with $N = 2, 3, 4, 6$ sensors are shown in Figures 10, 11, 12 and 13 respectively.

Figures 10-13 provide a clear understanding of the characteristics of the design space, but an optimal design point is not evident as there are trade-offs to be taken into account. As seen in these design spaces, a point with higher coverage can lead to larger average errors. Although increasing the number of sensors increases the performance of the cluster in terms of coverage and average error, configurations with additional sensors result in increased costs.
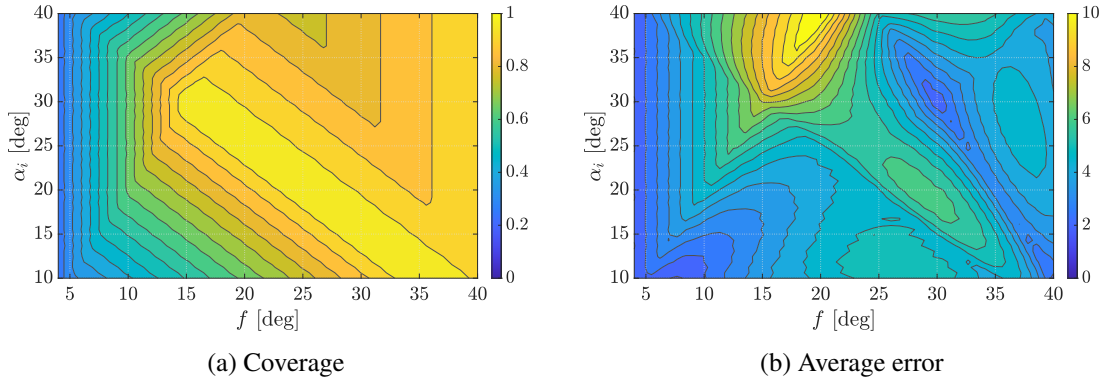
(a) Coverage (b) Average error

Figure 11: Design space for a cluster concept of three x-ray sensors

(a) Coverage (b) Average error
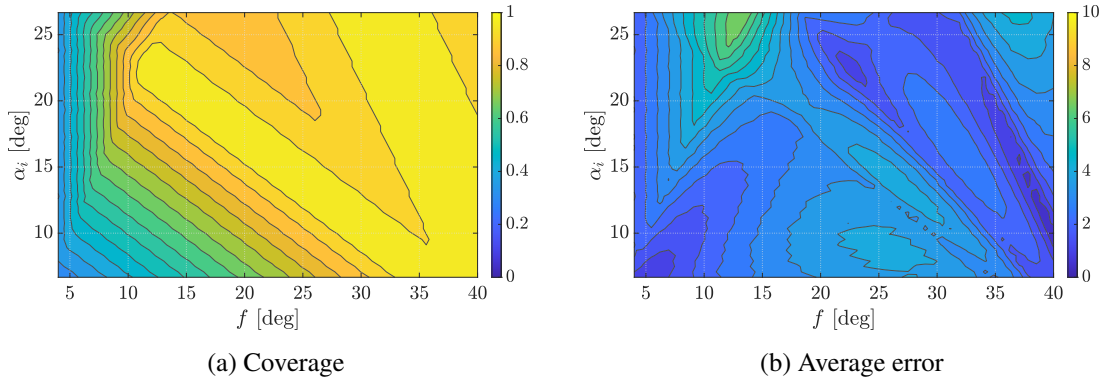
Figure 12: Design space for a cluster concept of four x-ray sensors

(a) Coverage (b) Average error
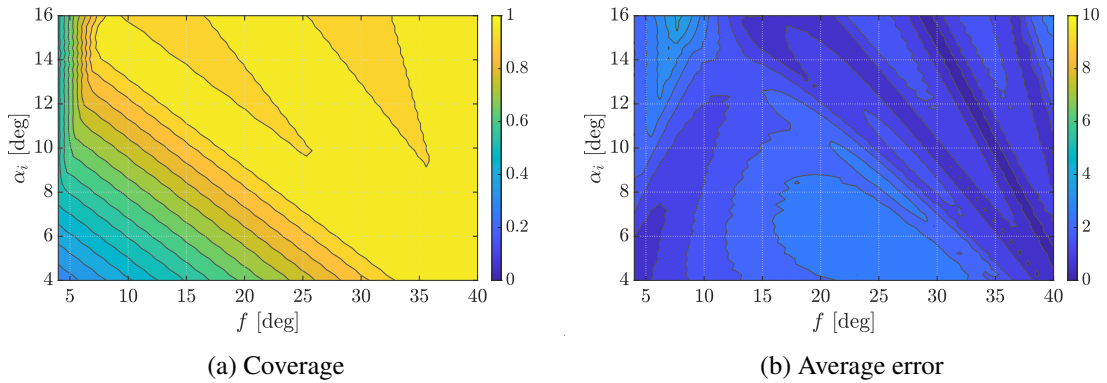
Figure 13: Design space for a cluster concept of six x-ray sensors

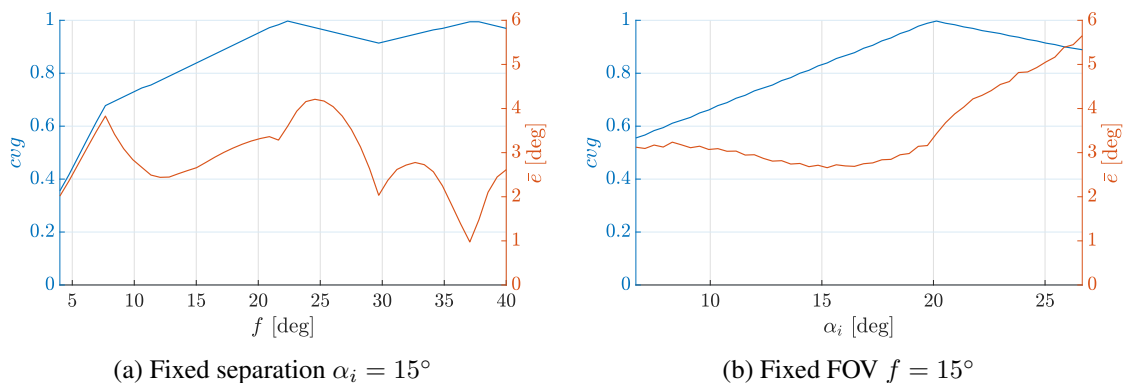(a) Fixed separation $\alpha_i = 15°$ (b) Fixed FOV $f = 15°$

Figure 14: Coverage and average error for a four-sensor cluster

Discussion of results

The analysis performed in this section shows that there are no benefits to a pyramid, sun sensor-like configuration. Because of the circular motion of the cluster platform, the ideal configuration is one in which the sensors are distributed in elevation. For a given number of sensors, whether coverage or average error in the area covered are the main driver for the desired application, different design points in terms of sensor field of view and overlap may be selected. A closer look at the four-sensor configuration design space is provided in Figure 14. It is evident here that there is a trade-off in the design space between maximizing coverage and minimizing average error. Therefore, the most advantageous design point will have to be selected depending on the application in hand.

It is also worth mentioning that the positioning of the sensors around the normal to the platform plays a major role in the acquisition of signals. Because of the circular motion of the platform, a sensor with a field of view containing $\boldsymbol{n}_P$ (*e.g.,* sensor with $f = 15°$, pointed at $\phi = 80°$) will not be able to detect a target in a cone around $\boldsymbol{n}_P$ (in the given example, a $5°$ half-angle cone). As the sensor rotates around $\boldsymbol{n}_P$, the aforementioned cone will always be within the field of view of the sensor, thus not generating any trigger events. Even when placing a sensor such that the edge of its field of view aligns with $\boldsymbol{n}_P$, the exact direction of $\boldsymbol{n}_P$ is unobservable. It is therefore not possible to avoid $\boldsymbol{n}_P$ becoming unobservable, and given that in the discussed configurations $\boldsymbol{n}_P$ aligns with what was defined as the preferred direction, this is a significant disadvantage of the present instrument concept.

Note that analyzing the design spaces in Figures 10-13, when increasing the FOV of the sensors past a certain point the coverage not only ceases to improve but begins deteriorating. This is also evident in Figure 14a. There are two factors that contribute to this effect. First, the area of interest considered here is the upper hemisphere, meaning that if a sensor covers an elevation angle below $0°$, this is not included in the coverage computation. Second, when $\boldsymbol{n}_P$ is inside the field of view of a sensor, increasing the field of view increases the blind spot created around this direction, reducing thus the coverage. Regarding average error, increasing the field of view at a fixed separation angle increases the overlap, but having an overlap of more than two sensors does not result in any improvement. Increased field of view also results in an enlarged area without overlap for the two sensors in the extremes, increasing thus the area in which the problem is under-determined and the errors associated with it.

A similar analysis can be done for increasing separation angles α_i at a fixed field of view (Figures 10- 13 and Figure 14b). The coverage increases up to the point where the upper sensor reaches n_P, then decreases. The minimum average error occurs for configurations with continuous two-sensor overlap in the central band (*e.g.,* for four sensors, $f = 15°$, $\alpha_i = 15°$). Reducing this separation reduces the central band, and increasing it beyond this point creates areas without overlap between sensors.

MULTIPLE CLUSTERS

Because the preferred direction for the instrument is always a blind spot, and in an effort to increase the coverage around the spacecraft, a number of instrument concepts with multiple x-ray clusters have been analyzed. In order to compare cases that would entail a similar production cost, a limited number of twelve x-ray sensors have been assumed to be available. The arrangements considered are 6 two-sensor clusters, 4 three-sensor clusters, 3 four-sensor clusters or 2 six-sensor clusters. To simplify the problem, each of the clusters in an instrument concept are assumed to be identical, *e.g.,* for a 3 four-sensor cluster instrument concept, each of the four-sensor clusters are equally defined with respect to their platform in terms of sensor pointing and field of view.

One of the main motivations for this approach is improving the performance of the instrument in the direction normal to the spacecraft side on which the instrument is mounted. To ensure this objective is accomplished, the clusters are positioned such that the blind spots of a cluster are covered by other clusters, and the preferred direction is in the area of coverage of multiple clusters. For all cases studied here, the design point selected is individual field of view $f = 15°$, and separation between sensors $\alpha_i = 15°$. This design point maintains a low average error for $N = 2, 3, 4, 6$. Even though the coverage at this point is relatively low, particularly for $N = 2, 3$, this disadvantage will be resolved with the inclusion of additional clusters.

The construction of each cluster with respect to their individual platform is as follows. The sensors are staggered in elevation such that $\phi = 0°$ (with respect to the platform plane) is the lowest angle covered. The sensors have a continuous two-sensor overlap in the central band. This means that the blind spot, if existing, is around the normal to the platform n_P. Table 4 contains the elevation angles for the four study cases analyzed here. This cluster configuration implies that, for clusters that do not cover the whole hemisphere ($N = 2, 3, 4$), the unobservable area forms a cone of half angle $f_{unobservable} = \frac{\pi}{2} - f(N + 1)$ around the platform normal.

Table 4: Elevation angles of x-ray sensors with respect to platform for multiple cluster study cases

N	ϕ_1 [deg]	ϕ_2 [deg]	ϕ_3 [deg]	ϕ_4 [deg]	ϕ_5 [deg]	ϕ_6 [deg]
6	15	30	45	60	75	90
4	15	30	45	60	-	-
3	15	30	45	-	-	-
2	15	30	-	-	-	-

In order to achieve the desired results, the cluster platforms are placed according to the following geometric constraint:

$$n_{P,k}^T n_{P,k+1} = \cos \beta_P \tag{9}$$

where $n_{P,k}$, $n_{P,k+1}$ are the unit normals of two consecutive cluster platforms and β_P is the angu-
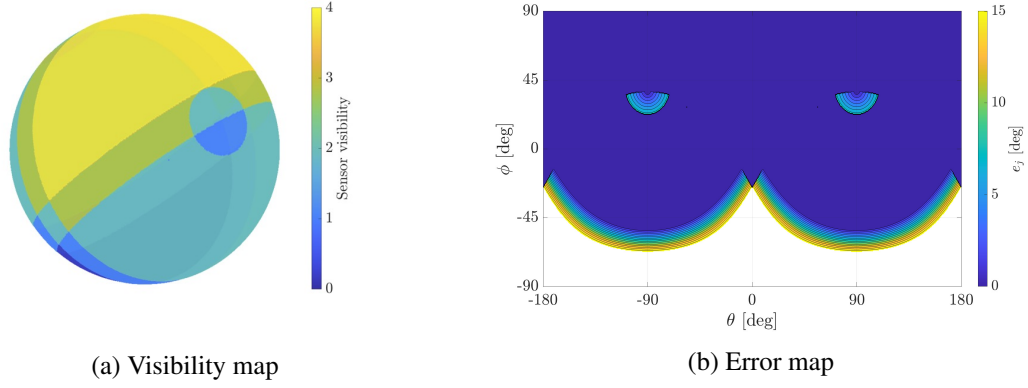
(a) Visibility map

(b) Error map

Figure 15: Visibility and error maps for an instrument concept of two clusters of six x-ray sensors

lar separation between them. The optimal separation angle is defined here such that the unobservable area of one cluster is fully covered by all other clusters.

$$\beta_{P,opt} = f(N+1) \tag{10}$$

The pointing of each platform with respect to the spacecraft side panel in which is mounted is

$$\boldsymbol{n}_{P,k} = \begin{bmatrix} \cos\theta_{P,k}\sin\varphi_P \\ \sin\theta_{P,k}\sin\varphi_P \\ \cos\varphi_P \end{bmatrix} \tag{11}$$

with $\theta_{P,k} = \frac{2\pi}{C}(k-1)$, $k = 1,\ldots,C$ (C being the number of clusters) the azimuth angle with respect to the spacecraft side and φ_P the angle with respect to the spacecraft side normal. The angle φ_P is obtained from Equation 9. Each of the clusters is then rotating about its platform normal at a constant speed ω.

Study case: two six-sensor clusters

For a case with two six-sensor clusters the optimal separation angle is $\beta_P = f(N+1) = 105°$. The two cluster platforms are therefore positioned with $\varphi_P = 52.5°$ (which corresponds to one half of the angular separation) and $\theta_P = 0°$ and $180°$ respectively. Figure 15a shows how many sensors can view a given point in a unit sphere around the spacecraft, and Figure 15b shows the errors obtained in the deterministic case. The areas with $e_j > 0$ correspond with areas in which only one sensor has visibility, meaning only two unique measurements can be obtained and the problem is under-determined. As seen in these Figures, the coverage is greatly improved with respect to the one cluster case. Since the coverage goes beyond one hemisphere, this metric together with average error are redefined in this section for a full sphere, $[-180°, 180°] \times [-90°, 90°]$ in azimuth and elevation. The coverage obtained in this study case is $cvg_{2c,sph} = 0.705$ and the average error in the area covered $\bar{e}_{2c,sph} = 1.41°$.

Study case: three four-sensor clusters

This study case presents three clusters with separation $\beta_{P,opt} = 75°$. The pointing of the cluster platforms is, with $\beta_{P,opt}$, $\varphi_P = 44.7°$ and $\theta_P = 0°$, $120°$ and $240°$ respectively. The results of

(a) Visibility map
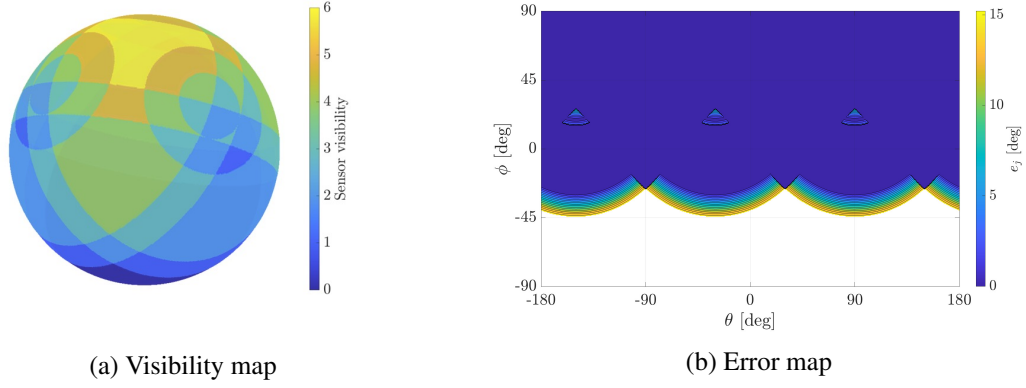

(b) Error map

Figure 16: Visibility and error maps for an instrument concept of three clusters of four x-ray sensors
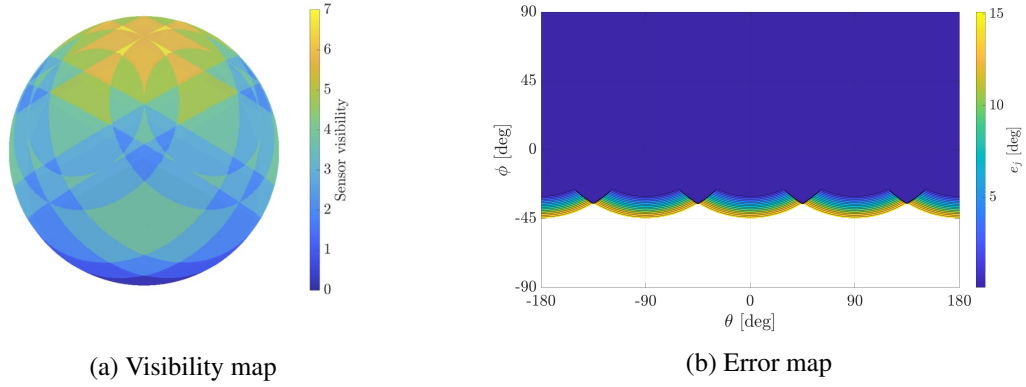

(a) Visibility map

(b) Error map

Figure 17: Visibility and error maps for an instrument concept of four clusters of three x-ray sensors

coverage map and error map are shown in Figure 16. For this study case, the coverage obtained is $cvg_{3c,sph} = 0.715$ and the average error in the area covered $\bar{e}_{3c,sph} = 1.05°$. Both metrics present a slight improvement compared to the two cluster study case.

Study case: four three-sensor clusters

For a case with four three-sensor clusters, the optimal separation angle is $\beta_{P,opt} = 30°$. With this separation angle, the pointing of the platforms is $\varphi_P = 45.0°$ and $\theta_P = 0°, 90°, 180°$ and $270°$ respectively. The errors and coverage plots are shown in Figure 17. The coverage obtained for this study case is $cvg_{4c,sph} = 0.732$, and the average error for the area covered is $\bar{e}_{4c,sph} = 0.94°$. This presents a slight improvement from the previous study case with three clusters.

Study case: six two-sensor clusters

For this case with six two-sensor clusters, the optimal separation angle between clusters is $\beta_{P,opt} = 45°$. This means the following positioning for the cluster platforms: $\varphi_P = 50.4°$ and $\theta_P = 0°, 60°, 120°, 180°, 240°$ and $300°$. The coverage and error maps are shown in Figure 18. The full sphere coverage obtained for this configuration is $cvg_{6c,sph} = 0.769$, and the average error for the deterministic problem is $\bar{e}_{6c,sph} = 0.76°$. These results present again a slight improvement with respect
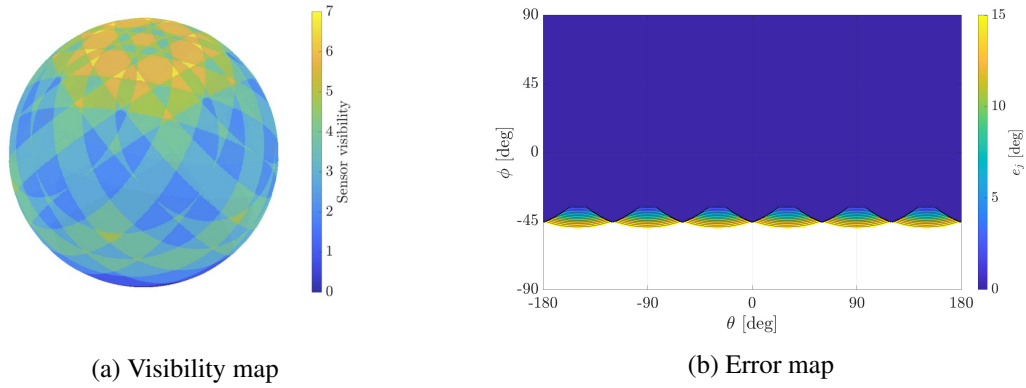
(a) Visibility map

(b) Error map

Figure 18: Visibility and error maps for an instrument concept of six clusters of two x-ray sensors

to the previous case study.

Discussion of results

This section introduces a set of multiple clusters variations for 12 x-ray sensors. The main objective of doing so is avoiding the existence of blind spots around the preferred direction of the instrument, which in Figures 15-18 corresponds to $\phi = 90°$. Increasing the coverage area and reducing the areas in which the problem is under-determined are secondary objectives. It has been confirmed here that the presence of additional clusters can result in a performance improvement that fulfills those objectives.

Figure15b and Figure 16b show how, for the two cluster and three cluster cases, there are areas in the upper hemisphere in which the problem is under-determined, resulting in small errors in the target heading. If this is not an acceptable result for a given application, the separation angle between clusters can be reduced, leading to a consequent reduction of the coverage area. The four cluster and six cluster configurations do not present this disadvantage, and therefore if small errors in the upper hemisphere were acceptable for the application, increasing the angular separation of the clusters could be explored in order to increase coverage.

In general, for a given number of sensors, increasing the number of clusters in which they are distributed improves both the coverage and average error metrics. Note that in the study of a single cluster, the area of interest was defined as the upper hemisphere, while for multiple clusters is the full sphere around a spacecraft. All study cases here provide a full coverage of the upper hemisphere and beyond, with the four three-sensor cluster and six two-sensor cluster options providing an average error in the upper hemisphere of $0°$. However, it is worth keeping in mind that additional clusters imply an increased number of moving parts and complexity, and a subsequent cost increment.

Note that this analysis has not considered possible occlusions of the field of view of the instrument from surfaces such as spacecraft solar panels or the spacecraft geometry itself. If the coverage goal goes beyond 2π sr this consideration is particularly important. This instrument concept is contingent on the orientation of the clusters, but there are no particular requirements on their location or distance to each other. Placing the clusters at advantageous locations (*e.g.,* the edge of a spacecraft side panel) can lead to coverage results similar to the results obtained here, but a more in depth analysis of the particular geometry is required.

CONCLUSIONS

This work investigates the use of x-ray sensors to detect an object in the vicinity of a spacecraft by exploiting the natural plasma interactions in the space environment. The scope of this paper is to analyze potential sensor configurations mounted on a rotating platform and characterize their effectivity. In this case, a simplified model of a single point stationary target is employed, in which the measurements are generated by *acquisition/loss of signal* events.

The design space for a fixed number of sensors in analyzed, using *coverage* and *average error* as performance metrics, and *field of view* of a sensor and *angular separation* between sensors as design parameters. In general, the optima for the two performance metrics occur at different design points, and therefore the optimal solution needs to be selected according to the requirements of the application. Note that the circular motion of the platform implies that the direction normal to the platform is always unobservable.

An additional exercise was performed by considering the case of a multi-cluster instrument concept. For this, a number of study cases were analyzed where a fixed number of 12 sensors is distributed in 2, 3, 4, or 6 identical clusters. By including additional clusters, the deficiencies of a single cluster are easily resolved, reaching 3π sr of coverage. Self-occlusions by the observer spacecraft have not been considered in this coverage computation.

ACKNOWLEDGMENTS

REFERENCES

[1] B. Lal, A. Balakrishnan, B. M. Caldwell, R. S. Buenconsejo, and S. A. Carioscia, "Global Trends in Space Situational Awareness (SSA) and Space Traffic Management (STM)," *Institute for Defense Analyses Science & Technology Policy Institute*, 2018.

[2] B. A. Corbin, A. Abdurrezak, L. P. Newell, G. M. Roesler, and B. Lal, "Global Trends in On Orbit Servicing, Assembly and Manufacturing (OSAM)," *Institute for Defense Analyses Science & Technology Policy Institute*, 2020.

[3] S. Kaplan, "Eyes on the Prize. The Strategic Implications of Cislunar Space and the Moon," 2020, p. 4.

[4] K. T. Wilson, M. T. Bengtson, and H. Schaub, "X-ray Spectroscopic Determination of Electrostatic Potential and Material Composition for Spacecraft: Experimental Results," *Space Weather*, Vol. 18, No. 4, 2020, p. e2019SW002342.

[5] K. Wilson and H. Schaub, "X-ray spectroscopy for electrostatic potential and material determination of space objects," *IEEE Transactions on Plasma Science*, Vol. 47, No. 8, 2019, pp. 3858–3866.

[6] J. Hammerl, Á. Romero-Calvo, A. López, and H. Schaub, "Touchless potential sensing of complex differentially-charged shapes using X-rays," *AIAA SciTech 2022 Forum*, 2022, p. 2312.

[7] G. H. McCall, "Calculation of X-ray bremsstrahlung and characteristic line emission produced by a Maxwellian electron distribution," *Journal of Physics D: Applied Physics*, Vol. 15, May 1982, pp. 823–831, 10.1088/0022-3727/15/5/012.

[8] J. Trincavelli and G. Castellano, "The prediction of thick target electron bremsstrahlung spectra in the 0.25–50 keV energy range," *Spectrochimica Acta Part B: Atomic Spectroscopy*, Vol. 63, Jan. 2008, pp. 1–8, 10.1016/j.sab.2007.11.009.

[9] A. Sicard-Piet, S. Bourdarie, D. Boscher, R. H. Friedel, M. Thomsen, T. Goka, H. Matsumoto, and H. Koshiishi, "A new international geostationary electron model: IGE-2006, from 1 keV to 5.2 MeV," *Space Weather*, Vol. 6, No. 7, 2008, pp. 1–13, 10.1029/2007SW000368.

[10] J. H. Schmitt, S. L. Snowden, B. Aschenbach, G. Hasinger, E. Pfeffermann, P. Predehl, and J. Trümper, "A soft X-ray image of the Moon," *Nature*, Vol. 349, No. 6310, 1991, pp. 583–587, 10.1038/349583a0.

[11] J. R. Wertz, "Attitude hardware," *Spacecraft Attitude Determination and Control*, pp. 155–216, Springer, 1978.

[12] S. A. O'Keefe and H. Schaub, "Sun-direction estimation using a partially underdetermined set of coarse sun sensors," *The Journal of the Astronautical Sciences*, Vol. 61, No. 1, 2014, pp. 85–106.

[13] J. Benton, "Pyramid Coarse Sun Sensing for NASA SSTI" Clark" Safe-Hold Mode," 1996.

[14] J. P. Snyder, *Map projections–A working manual*, Vol. 1395. US Government Printing Office, 1987.